

Article

Investigation of the Impact of an Electric Field on Polymer Electrolyte Membranes for Fuel Cell Applications

Hamdy F. M. Mohamed ^{1,*}, Esam E. Abdel-Hady ¹, Mohamed H. M. Hassanien ² and Wael M. Mohammed ¹

¹ Physics Department, Faculty of Science, Minia University, Minia P.O. Box 61519, Egypt; esamhady@mu.edu.eg (E.E.A.-H.); waelmohamed@mu.edu.eg (W.M.M.)

² Basic Science Department, Faculty of Engineering, Nahda University, New Beni Suef P.O. Box 62513, Egypt; mohammed.hamdy@nub.edu.eg

* Correspondence: hamdy.farghal@mu.edu.eg or hamdyfm@gmail.com; Tel.: +20-1208281849

Abstract: A systematic study was carried out on Nafion[®] 112 membranes to evaluate the effects of different electric field strengths on the structural and electrical properties of the membranes. The membranes were subjected to different electric field strengths (0, 40, 80, and 140 MV/m) at a temperature of 90 °C. Proton conductivity was measured using an LCR meter, revealing that conductivity values varied with the electric field strengths, with the optimal conductivity observed at 40 MV/m. Positron annihilation lifetime (PAL) spectroscopy provided insights into the free volume structure of the membranes, showing an exponential increase in the hole volume size as the electric field strength increased. It was also found that the positronium intensity of the Nafion[®] 112 membranes was influenced by their degree of crystallinity, which decreased with higher electric field strengths. This indicates complex interactions between structural changes and the effects of the electric field. Dielectric studies of the membranes were characterized over a frequency range of 50 Hz to 5 MHz, demonstrating adherence to Jonscher's law. The Jonscher's power law's *s*-parameter values increased with the electric field strength, suggesting a transition from a hopping conduction mechanism to more organized ionic transport. Overall, the study emphasizes the relationship between the free volume, crystallinity, and macroscopic characteristics, such as ionic conductivity. The study highlights the potential to adjust membrane performance by varying the electric field.

Keywords: Nafion[®] 112; polymer electrolyte membrane; fuel cell; electric field; conductivity; positron annihilation spectroscopy



Citation: Mohamed, H.F.M.; Abdel-Hady, E.E.; Hassanien, M.H.M.; Mohammed, W.M. Investigation of the Impact of an Electric Field on Polymer Electrolyte Membranes for Fuel Cell Applications. *Physics* **2024**, *6*, 1345–1365. <https://doi.org/10.3390/physics6040083>

Received: 1 October 2024

Revised: 17 November 2024

Accepted: 27 November 2024

Published: 17 December 2024



Copyright: © 2024 by the authors. Licensee MDPI, Basel, Switzerland. This article is an open access article distributed under the terms and conditions of the Creative Commons Attribution (CC BY) license (<https://creativecommons.org/licenses/by/4.0/>).

1. Introduction

The common knowledge of the environment has grown in response to alarming climate events in recent years, such as pollution and rising sea levels. Due to the enormous need for transportation, fossil fuels are predicted to run out for 2070 [1]. As a result, efforts to develop alternative energy sources are intensifying. The majority of renewable energy sources, on the other hand, are sporadic, resulting in gaps in the relationship between the supply and demand of energy, both spatially and temporally. Therefore, developing appropriate energy storage devices for the electrical grid is imperative [2]. For these uses, combining fuel cells with water electrolysis represents a potential path. With a theoretical conversion rate of 90%, fuel cells based on hydrogen show high promise as an energy source since all the fuel they require to produce energy is converted from chemical energy to electric energy [1].

Recently, interest in fuel cell technology has grown, particularly in proton exchange membrane fuel cells (PEMFCs). PEMFCs hold high potential as clean energy solutions due to their elevated power density, significant energy density at low operating temperatures, and compatibility with portable and stationary electronic devices [3]. In the PEMFC, the electrolyte membrane is made from a polymer [4–6]. This solid structure significantly

minimizes the risk of the electrolyte leaking into other layers. Two commonly known examples of commonly used PEMFC materials are Nafion[®] 112 membranes and Aquivion[®] perfluorosulfonated solid-state electrolytes [7–9]. There have been reports of the benefits of perfluorosulfonated polymers, including their hydrophilic sulfonic acid groups, hydrophobic PTFE (polytetrafluoroethylene) backbone, phase shift in the hydrated state, superior conductivity of protons, and so on [10,11]. Proton exchange membranes (PEMs) are the fundamental parts of fuel cells. PEMs separate the gases at the anode and cathode to reduce the possibility of direct contact and possible explosions. For a reaction, a PEM moves the produced H⁺ from the anode to the cathode. Therefore, it is necessary to have a meager gas penetration rate.

A PEM requires a specific level of mechanical strength to withstand hot and humid environments. Additionally, effective proton transmission necessitates high proton conductivity. A PEM that possesses these characteristics is considered exceptional. Nafion[®] is known for its outstanding performance as a PEM; however, its perfluorinated structure complicates its development and production [4,8,12]. This structure also compromises mechanical strength at elevated temperatures, resulting in high production and retail costs for Nafion. Pore filling has become a common method for enhancing the stability of Nafion[®] membranes. Haolin Tang and his collaborators at Wuhan University of Technology immersed Nafion[®] in a chemically modified solution of expanded polytetrafluoroethylene (ePTFE) [13]. This process aimed to improve the stability of the fuel cell by filling the backing material. Additionally, Mohanraj Vinothkannan and collaborators [14] explored the use of sulfonic acid-functionalized, unzipped graphite nanofiber (SO₃H-UGNF) as a potential filler for Nafion[®], creating a composite membrane intended for high-temperature hydrogen–air fuel cells (HAFCs). Another innovative approach to increase efficiency is the alteration of the membrane using an electric field. For the first time, Hsiu-Li Lin and collaborators [15] applied an electric field to the solid polymer Nafion[®] and observed an enhancement in the membrane's proton conductivity. The internal electric field of a fuel cell plays crucial roles in influencing power generation, efficiency, and overall system performance.

Understanding the factors that generate electric fields is essential for improving fuel cell architecture, enhancing efficiency, and addressing issues related to lifetime and functionality. Several key factors influence the generation of electric fields. (i) Ion transit. The movement of ions through the electrolyte is a critical factor in the production of electric fields. The ion transport properties of these electrolytes significantly affect the fuel cell's ability to generate electric fields [16]. (ii) Electrochemical reactions. The oxidation of fuel and the reduction of oxygen at the anode and cathode create these reactions, which are vital for the fuel cell's operation. (iii) Interfaces and catalysts. Catalysts are necessary at these interfaces to facilitate electrode reactions and improve the overall efficiency of the fuel cell system [17]. (iv) Cell geometry and design. The configurations of the electrodes, flow channels, and current collectors can impact how the electric field is distributed within the fuel cell. Advancing the understanding in the areas helps to develop more reliable and efficient fuel cell devices, paving the way for broader applications of this sustainable and clean energy source. However, it is to stress that the electric fields in PEMs can alter proton conductivity, affect membrane stability, and lead to structural changes.

It is of high importance to understand how electric fields influence PEMs in order to maximize fuel cell efficiency and address challenges related to membrane degradation, water management, and durability. PEMs can undergo morphological changes due to electric fields, which can alter their composition and properties. These changes include the initial interactions of PEM with electric fields, which can lead to changes in ion cluster formation, membrane expansion or contraction, and alterations in the conformation of the polymer backbone. Electric fields can have a significant impact on the proton conductivity of a PEM. They can affect proton hopping kinetics, the formation of proton transport channels, and the levels of proton hydration. These can ultimately influence the overall proton conductivity of the PEM, impacting the performance of the fuel cell, particularly under high current densities or varying humidity conditions [18,19]. Moreover, electric

fields can exacerbate mechanisms of membrane degradation, such as chemical breakdown, mechanical stress, or electrochemical oxidation. This can accelerate the aging process of membranes, reducing their lifespan and functionality. Therefore, a comprehensive investigation into the effects of electric fields on membrane degradation is necessary to develop strategies to prevent or mitigate these adverse consequences [20].

Thus, the first step in a microstructure analysis is to estimate the free volume inside the membranes using positron annihilation lifetime (PAL) spectroscopy [21–23]. The free volume at the nanoscale seen in the polymer matrix and the molecular materials' transport kinetics of molecules (gas/methanol) both influence the mechanism of proton conductivity. The free volume concept of molecule permeation and ionic conductivity states that ionic conductivity and molecular diffusion are made possible by the free volume, which is symbolized by sub-nanometer-sized holes in the polymer amorphous domain [24,25]. For molecules like H_2/O_2 or methanol/ O_2 , it is asserted that the structure of membranes with a higher size of the free volume have high permeability and strong conductivity, according to the free volume model [26]. In our earlier studies [8,27], at enough high temperatures, we found significant relationships between permeability and proton conductivity and the free volume holes produced by PAL methods. These results indicated that the free volume is a determining factor for both gas permeability and the protonic conductivity in the Nafion[®] membrane. PEMs derived from hydrocarbons or perfluorocarbons often show destructive anisotropy or isotropic conductivity, which indicates that PEM's proton conductivity is lower when moving out of the plane than when it is in. However, the relationships obtained feature a fast base with an incredible phase-separated shape, as well as tortuous-path conductive channels [28,29]. Generally, the fuel cell execution can be improved by increasing the transport efficiency of the protons from the anode to the cathode through a conduit with a shorter or substantially lower bending conductance into the out-of-plane channel.

To date, as noted in the review [30], the conductivity of Nafion[®] membranes has been oriented in the “out-of-plane” direction through electric field-driven alignment. The current study focuses on the effects of electric fields on Nafion[®] membranes. We give a comprehensive analysis of the processes that generate electric fields in fuel cells and examine how these processes influence the essential characteristics of the polymer electrolyte membranes used in the fuel cells. By applying an external electric field to Nafion[®] membranes at a fixed temperature—ranging between the melting point and glass transition temperature—molecular motion is energized. Therefore, in this study we measure proton conductivity and utilize the PAL technique to investigate the effects of various strengths of applied electric fields on the Nafion[®] 112 membrane at 90 °C. Additionally, the study establishes a correlation between the electrochemical properties of PEMs and their free volume nanostructure, as determined by the positron annihilation lifetime technique. This research examines the basic principles, underlying theories, and experimental data to enhance the understanding of the complex electrochemical processes that occur within fuel cells.

2. Experimental Setup and Data Analysis

The chemical structure of the Nafion[®] 112 membrane (DuPont, Wilmington, DE, USA) is depicted in Figure 1. Five samples with dimensions of 5 cm × 5 cm × 50 μm had been cut from one sheet and used right as supplied, without any chemical modification (denoted “as received” in what follows). To adjust the electric field strengths, the sample was placed between two electrodes in a sample holder connected to a high-voltage source. At a rate of 2 °C per minute, the Nafion[®] 112 membrane within the sample holder was heated in an oven from 30 °C to 90 °C. The temperature was dropped to 30 °C at the same rate after being held at 90 °C for an hour. The thermal progression from heating to collision takes about two hours. The high voltage for the electric field effect was set at fixed values during these two hours. The preceding process was carried out once more on the five samples to affect the membranes at different strengths of the electric field (0, 40, 80, and 140 MV/m). Next, each membrane sheet that had been treated was cut into the proper sizes

and shapes to match each measuring procedure. Before conducting the characterization measurements, the resulting membranes were stored for one month at room temperature to ensure that the membrane structure was proportionate to the electric field strengths and that the membrane properties did not change.

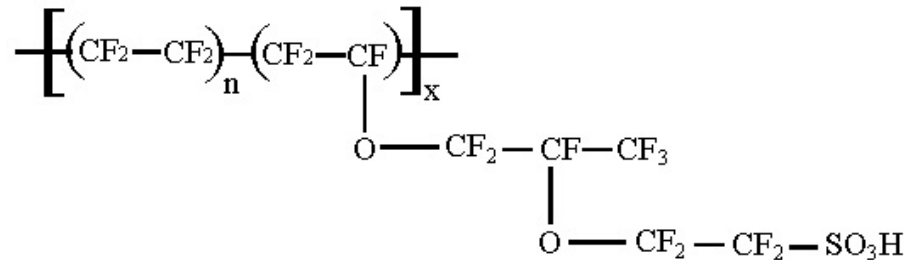


Figure 1. The chemical structure of the Nafion® 112 membrane.

Wide-angle X-ray diffraction (WAXD) was used to study the crystal structure of the present membranes using a Bruker (model D8) diffractometer with $\text{CuK}\alpha$ (with the wavelength $\lambda_X = 1.54184 \text{ \AA}$) incident radiation. The WAXD patterns were investigated in the 2θ range of 5° – 80° at 30°C , where θ represents the incident angle of the X-ray beam and a relative humidity of approximately 35%. The measurements were performed in the Central Laboratory of Microanalysis and Nanotechnology, Minia University, Egypt. The Hioki 3532 LCR meter was utilized to measure the conductance (G) of the membranes under study at 30°C and 35% relative humidity. The frequency range covered by the measurements was 50 Hz–5 MHz. Proton conductivity σ [31,32]

$$\sigma(\text{S/m}) = \frac{dG}{a}, \quad (1)$$

where d denotes the membrane thickness and a is the cross-sectional area of the cathode, was computed with 2% accuracy.

To create the positron source, about 20 μCi of aqueous $^{22}\text{NaCl}$ was placed on a thin sheet of Kapton foil (7 μm thick). The $^{22}\text{NaCl}$ spots were allowed to dry completely before being covered with a corresponding piece of Kapton foil, sealed with epoxy glue, and placed under a vacuum for one day. The Kapton foils absorb about 10% of the positron source, contributing to the components that have a short lifetime. This absorption was not distinguished by the PAL spectra analysis. The PAL data were evaluated in a vacuum at room temperature using a standard fast–fast coincidence setup [4,5,33]. The system's time resolution has been calculated by measuring the thick Kapton foils' PAL spectrum. It seems that the only polymer that does not have a long-lived component, or Ps yield, is Kapton [34,35]. Using RESOLUTIONFIT software (version 3.106), the resolution of the PAL approach was measured to be 240 ps, it mentions the full width at half maximum. Al foil was used to encase the membrane/positron source/membrane sandwich to carry out room temperature PALs measurements, or roughly at 30°C . The PAL spectrum with more than two million counts was deconvoluted into three lifetime-components using PALSfit3 software (version 3.251) [36,37]. The data analysis did not employ source correction. By utilizing an approved reference material, we were able to verify the accuracy of our measurements and the data analysis (The National Metrology Institute of Japan (NMIJ), certified reference materials (CRM 5601-a) [38,39].

Three positron states are found in polymeric materials: spin parallel ortho-positronium (o-Ps) with a lifetime τ_3 of about 1 to 10 ns, the spin antiparallel para-positronium (p-Ps) with a lifetime τ_1 of about 125 ps, and the free positron with lifetime τ_2 of about 450 ps [40]. The positron lifetimes in these states are characterized by their relative intensities I_1 , I_2 , and I_3 , respectively. The component of the o-Ps lifetime is one of the most essential PEM properties, even if the average hole volume size and the o-Ps lifetime τ_3 are related. On the other hand, the o-Ps intensity I_3 , which is dictated by the makeup of processes involving an

energetic positron, represents the probability of creation of o-Ps. In addition to structural alterations such as crystallinity [41] or membrane doping with NaI, an inhibitor of Ps creation [42], these processes may result in Ps formation or inhibition. The relationship between the average radius R of the hole volume and the o-Ps lifetime τ_3 is given in the Tao–Eldrup model [43,44] as follows:

$$\tau_3 = 0.5 \left[1 - \frac{R}{R_0} + \frac{1}{2\pi} \sin\left(\frac{2\pi R}{R_0}\right) \right]^{-1} \text{ ns}, \tag{2}$$

where o-Ps annihilates in a homogeneous electron layer with a thickness $\Delta R = 0.166$ nm and $R_0 = R + \Delta R$ [45,46]. Using the formula

$$V_{\text{o-Ps}} = (4/3)\pi R^3, \tag{3}$$

one can determine the hole volume size $V_{\text{o-Ps}}$ in nm^3 .

A complex expression of the PAL system resolution function $R(t)$, where t denotes the decay time, represented by a limited number n of negative exponentials, characterizes the observed positron lifetime data $y(t)$ as follows [37]:

$$y(t) = R(t) \left[N_t \sum_{i=1}^n (I_i/\tau_i) \exp(-t/\tau_i) + B \right]. \tag{4}$$

In Equation (4), the normalized count is denoted N_t , B stands for the background, and I_i ($\sum I_i = 1$) is the relative intensity of the positron lifetime τ_i . Each positron lifetime spectrum with a total of 3×10^6 counts was split into three lifetime components using PALSfit3 software (version 3.251) software. The entire data processing procedure made use of source rectification [47]. Given the assumption that the real values of the positron lifespan are made up of a continuous distribution instead of the previously mentioned more discrete circulation, the PAL spectrum can be expressed as a continuous decay as follows [48]:

$$y(t) = R(t) \left[N_t \int_0^\infty (I(\tau)/\tau) \exp(-t/\tau) d\tau + B \right], \tag{5}$$

where

$$\int_0^\infty I(\tau) d\tau = 1. \tag{6}$$

Here, N_t represents the PAL spectrum’s total count. Standard LT9.0 software was used to carry out the usual discrete term study [47,48]. The biggest advantage of LT9.0 programs is the ability to reduce the number of free parameters. This may be achieved in the LT9.0 program in various ways. The most straightforward one, which is already available in LT9.0, is to use a combination of two most reliable program features, namely (a) multiple spectra analysis, and (b) so-called “parameter statuses”, which define various kinds of constraints imposed on the parameters. Analyzing multiple spectra brings the advantage of finding common values for chosen parameters. Such processing makes the resulting value more reliable in the case when one parameter should have the same value for all spectra. For the annihilation rates λ of positronium in the free volume, the normal distribution is considered, which equals $1/\tau_3$, as follows:

$$\alpha_3(\lambda) = -(2\pi)^{-0.5} \sigma_3^{-1} \exp \left[-\frac{(\ln \lambda - \ln \lambda_{30})^2}{2\sigma_3^2} \right] \lambda^{-1} d\lambda, \tag{7}$$

where σ_3 refers to the distribution dispersion and λ_{30} refers to the peak annihilation rate of positronium in free volumes. From this, the distribution of $\alpha_3(\tau_3)$ is given by

$$\begin{aligned} \alpha_3(\tau_3) &= -(2\pi)^{-0.5} \sigma_3^{-1} \exp\left[-\frac{(\ln \lambda - \ln \lambda_{30})^2}{2\sigma_3^2}\right] \lambda^{-1} d\lambda \frac{d\tau_3}{d\lambda} \\ &= -(2\pi)^{-0.5} \sigma_3^{-1} \exp\left[-\frac{(\ln \lambda - \ln \lambda_{30})^2}{2\sigma_3^2}\right] \lambda^{-1} d\tau_3. \end{aligned} \tag{8}$$

where λ_{30} refers to the peak annihilation rate of positronium in free volumes so that the free volume size distribution $\alpha_3(V)$ is expressed as

$$\alpha_3(V) = -(2\pi)^{-0.5} \sigma_3^{-1} \exp\left[-\frac{(\ln \lambda - \ln \lambda_{30})^2}{2\sigma_3^2}\right] \lambda^{-1} d\lambda \frac{dV}{d\lambda}, \tag{9}$$

where

$$\frac{dV}{d\lambda} = -\frac{4\pi R^2(R + R_o)^2}{2R_o} \left(1 - \cos\left(\frac{2\pi R}{R + R_o}\right)\right)^{-1}. \tag{10}$$

In disordered regions of the polymer matrix, the o-Ps trapping rate estimates were computed using bulk positron lifetime τ_b , as follows [49,50]:

$$\frac{1}{\tau_b} = \frac{I_1}{\tau_1} + \frac{I_2}{\tau_2} + \frac{I_3}{\tau_3}. \tag{11}$$

Assume that the term “free positron annihilation rate” refers to the positron annihilation in regions other than the open-volume defects. The reciprocal of the bulk positron lifetime, $\lambda = 1/\tau_b$, is the free positron annihilation rate. However, the mean lifetime τ_m can be expressed as follows:

$$\tau_m = \frac{\tau_1 I_1 + \tau_2 I_2 + \tau_3 I_3}{I_1 + I_2 + I_3}. \tag{12}$$

Nevertheless, the mean positron lifetime is sensitive to all the parameters pertaining to the annihilation states and atomic characteristics of the sample, regardless of the number of components resolved in the PAL spectrum.

As per the model by Oleh Shpotyuk and colleagues [51], the positron and Ps may become caught in two different kinds of defects. The trapping rates in the respective free volume of membranes are denoted as K_{d1} and K_{d2} [50], namely the positron annihilation rate in the crystalline region is defined as

$$K_{d1} = I_2 \left(\frac{1}{\tau_1} - \frac{1}{\tau_2}\right), \tag{13}$$

and the Ps annihilation rate in free volume holes is defined as

$$K_{d2} = I_3 \left(\frac{1}{\tau_1} - \frac{1}{\tau_3}\right). \tag{14}$$

The positron trapping rate (V_+) in the ordered or crystalline portion of the membrane can be obtained using the following relation [52]:

$$V_+ = \frac{3I_2 \left(\frac{1}{\langle \tau_b \rangle} - \frac{1}{\tau_2}\right)}{3I_1 - I_3}, \tag{15}$$

where $\langle \tau_b \rangle$ represents the average bulk positron lifetime τ_b for all the samples. However, the trapping rate of Ps (V_{Ps}) in the amorphous areas of the semicrystalline polymer can be calculated as follows [52]:

$$V_{Ps} = \frac{4I_3 \left(\frac{1}{\langle \tau_b \rangle} - \frac{1}{\tau_3}\right)}{3 - 4I_3 - 3I_2}. \tag{16}$$

3. Results and Discussion

Sulfone groups ($-\text{SO}_3^-$) and counterions (H^+) represent the functional groups of the Nafion[®] 112 membrane; combined, those groups create SO_3H , as exhibited in Figure 1. Concerning the influence of the electric field, it is exerted by the $-\text{SO}_3^-$ and H^+ dipoles of the Nafion[®] 112 membranes. The torque of the dipoles is $EQD \sin \phi$, where ϕ is the angle between the line connecting the two dipoles, E is the electric field lines, D represents the split in the poles, and $-Q$ or $+Q$ is the negative or positive charge in each segment of the dipole. A more complex scenario is required in real systems to explain the structural alterations, particularly at high temperatures (about 90 °C).

The PAL spectra of the Nafion[®] 112 membrane were deconvoluted into three lifetime components using the PALSfit and LT9.0 software [37,47]. At different electric field strengths and at 90 °C, the PAL spectra were acquired both “as received” and modified. There is a close agreement between the PAL parameters from the PALSfit analysis and the LT9.0 analysis. The components with the shortest and intermediate lifetimes, $\tau_1 \sim 0.13$ ns ($I_1 = 5\text{--}44\%$) and $\tau_2 = 0.42\text{--}0.52$ ns ($I_2 = 41\text{--}86\%$), originate from the p-Ps and free annihilation of positrons with an electron, respectively. These can include more than two contributions thanks to the complex polymer positron states and spur reactions [23]. The longest lifetime component ($\tau_3 = 2.44\text{--}2.75$ ns and $I_3 = 9\text{--}11.5\%$) may be owing to the o-Ps pick-off annihilation. The o-Ps lifetime τ_3 and its intensity I_3 of the as-received membrane and those with different field strengths at 90 °C are shown in Figure 2. Also, the free volume size $V_{\text{o-Ps}}$ is shown in Figure 2 which was determined using Equations (2) and (3). At a zero electric field strength, the sample hole volume size at 90 °C was less than its value at room temperature. As soon as heating the membrane causes the water to evaporate and the degree of crystallinity to rise, this suggests that the amorphous portion of the membrane decreases [7]. The free volume size increases with the strength of the electric field, suggesting an increase in the amorphous region due to an increase in the migration of the dipoles due to the strength of the applied field.

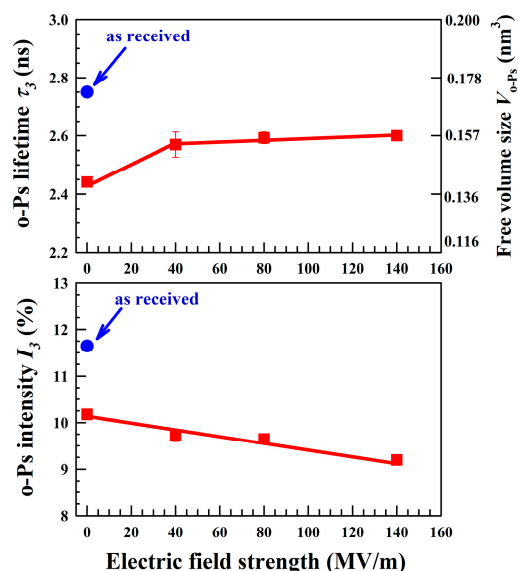


Figure 2. The o-Ps lifetime τ_3 , o-Ps intensity I_3 , and free volume size $V_{\text{o-Ps}}$ derived from Equations (2) and (3) as a function of the electric field strengths applied to Nafion[®] 112 membranes at 90 °C. The “as received” denotes the factory-supplied sample.

As mentioned just above, the Nafion[®] 112 membrane’s degree of crystallinity increases with heating to the point where the o-Ps intensity I_3 drops. The o-Ps intensity I_3 smoothly drops as the strength of the electric field increases at 90 °C. On the other hand, Figure 3A shows the WAXD pattern for the Nafion[®] 112 membrane as received, recorded at room temperature (30 °C) and a relative humidity of 35%. The current trend is comparable to the

findings of Ref. [22], where it is claimed that an amorphous hump that might be divided into two peaks exists over the range of $2\theta = 8^\circ$ – 24° . The crystalline domain is shown by the narrow peak, whereas the amorphous domain is identified by the wider peak. The hexagonal structure of polytetrafluoroethylene (PTFE)-like crystallites in Nafion can be represented by the (100) reflection of the peak [53]. Therefore, the decomposed WAXD pattern in the 2θ range from 8° to 24° can be used to determine the relative crystallinity and amorphous regions, as shown in Figure 3B–F. One can see that all of the current Nafion[®] 112 membranes under investigation are semicrystalline, with a degree of crystallinity in the range of 20–39%, as listed in Table 1. It is commonly known that the degree of crystallinity of the sample can be correlated with the o-Ps intensity I_3 , meaning that a lower o-Ps intensity I_3 is correlated with increased crystallinity [54]. This is not the case here, where the o-Ps intensity I_3 and the degree of crystallinity both decreases. Therefore, this change in I_3 is not caused by a modification in the hole number (hole volume content) in the membrane [55].

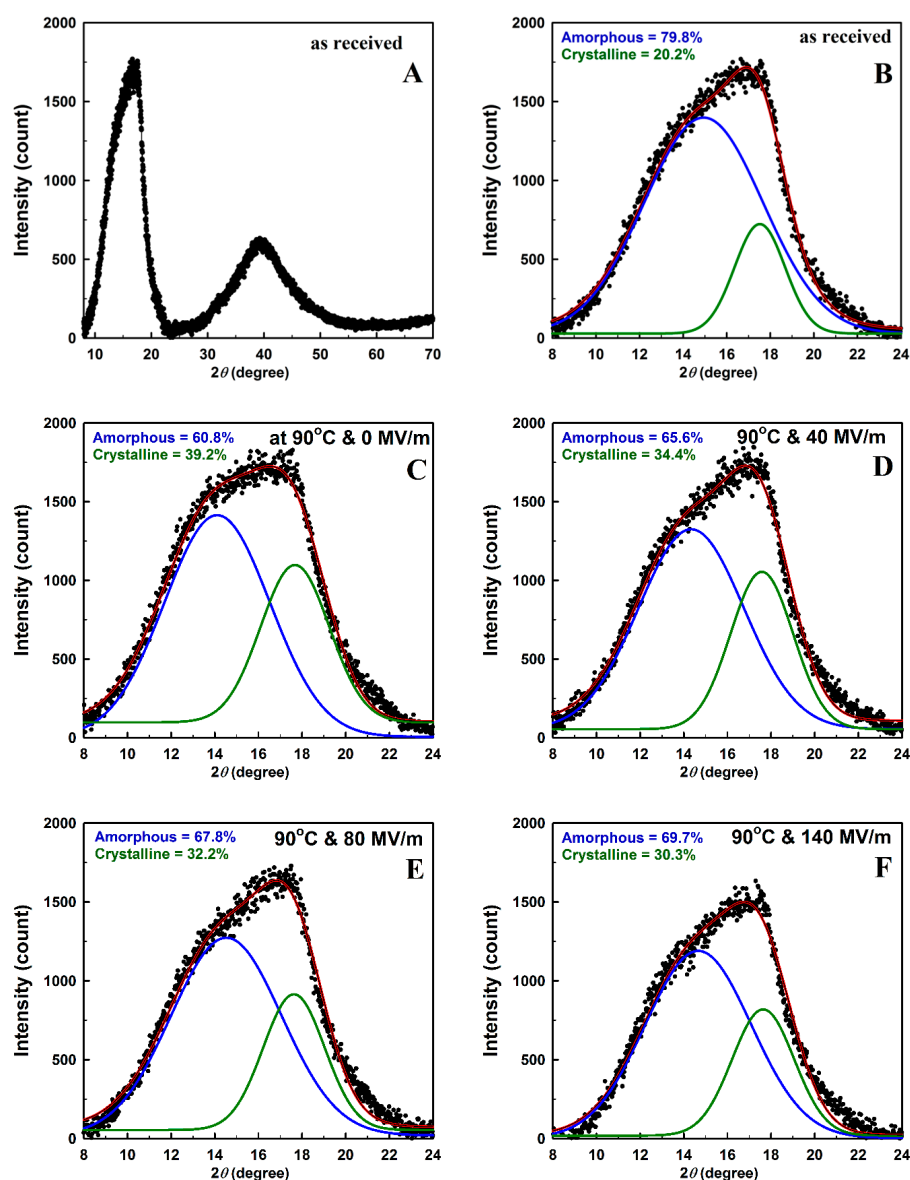


Figure 3. Wide-angle X-ray diffraction (WAXD) patterns for the as-received Nafion 112 membranes and those with different electric field strengths at 90 °C. The red line represents the fit of the experimental data.

Table 1. Variations in the degree of crystallinity with the electric field strength. The factory-supplied sample is denoted as “as received”.

Electric Field (MV/m)	Degree of Crystallinity (%)
as received	20.2
0	39.2
40	34.4
80	32.2
140	30.3

Furthermore, since the Nafion[®] 112 membrane is known to be a polar polymer, a spur model [56] may be utilized to interpret the findings. The spur model states that Ps is created when a thermalized positron and an electron that has been extracted from the material combine. Ps then develops following the complete thermalization of the positron and electron. Numerous events, the recombination of electrons and ions, as well as the positron and electron departing the spur, then compete with the reaction of the spur for Ps formation. Since this is a Coulomb reaction, it is known that there is little interaction between the electrons and positrons [57]. Certain electronegative groups—especially polar groups—may graft with the sample’s molecular chains during the electric field procedure. These polar groups may prevent Ps from forming, which would lower the intensity of o-Ps [58]. Therefore, the electron can be separated from the positron using an electric field, which also reduces the creation of Ps (reduced I_3).

It is commonly recognized that the free volume distribution of the materials is one of their main features. This distribution affects the materials’ properties and determines the crystal structure, mechanical stability, and membrane thermal stability. Figure 4 exhibits the free volume distribution of the membranes as received and at different electric field strengths. One can see that the free volume distribution moved to a larger free volume size as the electric field strength increased. An electric field associated with the deterioration effect caused the samples’ free volume distribution to alter, increasing the free volume size. Interesting information may also be obtained by examining the width of the free volume distribution. For the as-received sample, the free volume distribution was wider compared with that for the heated membrane at 90 °C, because of the decrease in the free volume size due to crystallinity or water removal. For the electric field effect, the free volume distribution got narrower with increasing the electric field strength. This indicates that the electric field effect turned to make the free volume size combine and form a free volume with almost of the same sizes.

Figure 5 shows the positron parameters, such as τ_m , τ_b , K_{d1} , K_{d2} , V_+ , and V_{Ps} , deduced from the analysis of the PAL spectra and Equations (11)–(16) for the present membranes. As demonstrated in Figure 5a, the mean positron lifetime τ_m showed a notable rise with increasing electric field intensity up to 40 MV/m, after which it dropped steadily. As already known [56], after entering a solid, positrons thermalize quickly (in less than 10 ps), which causes them to diffuse widely through the material until they eventually annihilate with electrons. Another consequence of positron diffusion in nanocrystalline materials is that the positrons will diffuse out to the surfaces since the size of the crystallite is smaller than the positron diffusion length (100 nm) [59]. The overlap of the positron wavefunction with the local electron density determines the lifetime of the positrons at the structural free volumes on the crystallite surfaces. The cumulative effect of the positrons entering the sample being annihilated is reflected in the positron mean lifespan indicated by Equation (12). The variation with the electric field intensities well illustrates the existence of electric field effects and shows how sensitive the positron annihilation spectroscopy (PAS) is to such electronic structural alterations. It was found that τ_m for the Nafio[®] 112 membrane in its as-received state was lower than its measured value after heating at 90 °C; this is related to the increased degree of crystallinity of Nafion[®] 112 after heating. This agrees with the study by Jerzy Dryzek [60], where it is stated that an increase in temperature induces the

creation of thermally activated monovacancy or crystals, which is reflected in the increase in the mean positron lifetime.

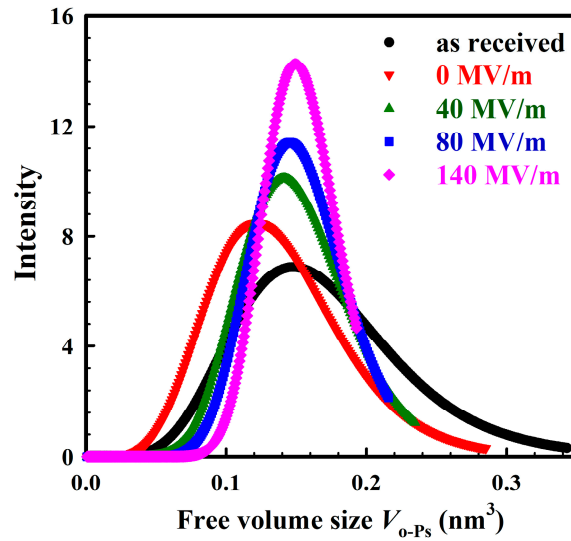


Figure 4. The free volume size distribution deduced using the LT9.0 program for the as-received Nafion[®] 112 membrane and those affected with different electric field strengths at 90 °C.

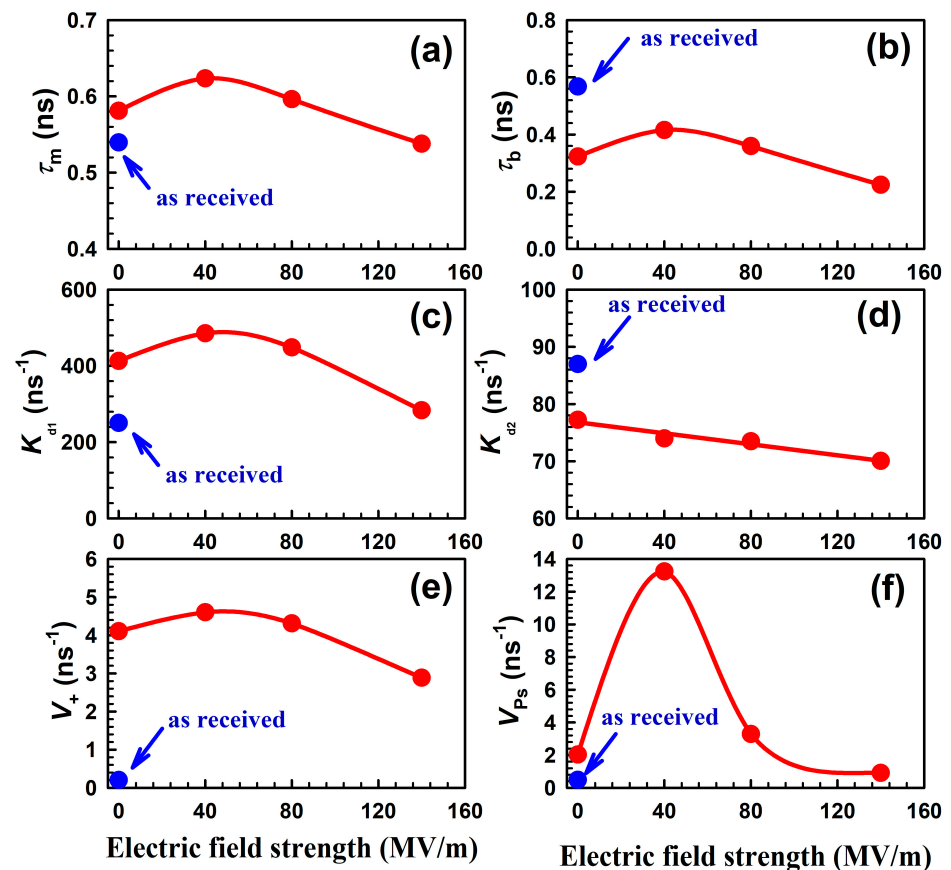


Figure 5. Variations of (a) τ_m (b) τ_b (c) K_{d1} (d) K_{d2} (e) V_+ and (f) V_{Ps} with the electric field strengths. See text for details.

Since it is a constant value for the materials and is associated with annihilations from the high crystalline regions in the membrane, the bulk positron lifetime is of highest importance. The behavior of the bulk positron lifetime τ_b with the electric field strengths,

as shown in Figure 5b, is like that of τ_m , which can be used for the same interpretation. Due to its inverse relationship with the electron density at the annihilation site, the bulk positron lifetime τ_b is known to reflect the electronic structure directly. In Ref. [61], it is shown that the relation between the electron densities n_0 (a.u.) and the bulk positron lifetime τ_b as follows:

$$\tau_b = 1/(2 + 134 n_0) \times 10^3 \text{ (ps)}. \quad (17)$$

Generally, the electron density in polymers such as Nafion[®] 112 increases with increasing temperature due to increasing crystallinity. Equation (17) requires that the positron lifetime generally decreases with increasing temperature (Figure 5b), while τ_b for the as-received membranes is as high as that heated at 90 °C. On the other hand, increases in the strengths of the electric field higher than 40 MV/m at 90 °C for Nafion[®] 112 membranes cause the production of a more amorphous area, which lowers the bulk positron lifetimes.

The investigated Nafion[®] 112 membranes exhibit two distinct types of traps, as illustrated in Figure 5c,d; the traps are the long-lived and short-lived ones with the K_{d1} and K_{d2} trapping rates, respectively, when $K_{d1} > K_{d2}$. Due to the semicrystalline nature of Nafion[®] 112, K_{d1} represents the positron annihilation rate in crystalline region defects, while K_{d2} represents the Ps annihilation rate in free volume holes. The role of long-lived locations for positron trapping or the amorphous region's trapping rate is strongly enhanced so that their trapping rate K_{d2} (70–77 ns⁻¹) becomes only 4–5 times less as for the crystalline region's trapping rate K_{d1} (283–485 ns⁻¹). The behavior of K_{d1} is almost the same as that of τ_m , while the behavior of K_{d2} is almost similar to the o-Ps intensity I_3 as a function of the electric field strengths. The trapping rate is impacted by both the chemical structure of the sample and the concentrations of defects.

The positron trapping rate V_+ in the membranes' vacancy-type defect is shown in Figure 5e. As observed in the figure, the behavior of V_+ against the electric field strengths is similar to that for τ_m and K_{d1} . So, the previous discussion about τ_m and K_{d1} can be used for the interpretation of the V_+ trend. On the other hand, Figure 5f presents the variation in the trapping rate of positronium V_{Ps} versus the field strengths. V_{Ps} increases with the electric field strength up to 40 MV/m, and then it decreases with the electric field strength. The trend of V_{Ps} is connected to the increase in the free volume size with electric field strengths; however, the change in the free volume size in the range of the electric field strength from 0 to 40 MV/m is larger compared with that in the range from 40 to 140 MV/m.

Any material behaves as the ideal Debye model if its Nyquist plot displays a complete semicircle with its center located on the real part of the impedance (Z' -axis) [62,63], which is described by the equation

$$\varepsilon^* - \varepsilon_\infty = \frac{\varepsilon_s - \varepsilon_\infty}{1 + j\omega\tau_l}, \quad (18)$$

where ε^* denotes the complex dielectric constant, ε_∞ denotes the permittivity's high frequency limit, ε_s denotes the permittivity's minimum frequency limit, τ_l represents the relaxation time, j denotes the imaginary unit refers to a phase shift in the complex plane, and ω denotes the angular frequency. For materials with a single relaxation time, this equation provides an excellent description of the relaxation phenomena. Their Nyquist plot for other materials displays a depressed semicircle with a center below the X-axis (real part of impedance). Since these materials have several relaxation times with different relaxation mechanisms, it is claimed that they have deviated from the ideal Debye model. Equation (18) is not sufficient to characterize the relaxation events for these materials [64,65]. In Ref. [66], another equation is suggested which can be used to show how the actual Debye behavior differs from the ideal one:

$$\varepsilon^* - \varepsilon_\infty = \frac{\varepsilon_s - \varepsilon_\infty}{1 + (j\omega\tau_l)^{1-\gamma}} \quad (19)$$

or the Nyquist equation [67]:

$$\varepsilon^* - \varepsilon_\infty = \frac{\varepsilon_s - \varepsilon_\infty}{\left[1 + (j\omega\tau_l)^{1-\gamma}\right]^\beta} \quad (20)$$

where τ_l measures how fast the material complies to changes in an applied electric field. The distribution of the relaxation times for this equation is represented by two parameters. The higher asymmetric distribution on the short-time side is defined by the γ parameter, whilst the spreading symmetrical distribution on the logarithmic scale is indicated by β . The fundamental building blocks of all these equations are the parameters β and γ , whose values range from zero to one. For $\gamma = 0$ and $\beta = 1$, the deviation is zero, and Equations (19) and (20) yield the Debye equation (Equation (18)). A departure from the ideal Debye model is found for $\gamma > 0$ [68].

Figure 6a exhibits the relation between the frequency versus the dielectric constant ε' of the as-received sample and after exposure to different strengths of the applied electric field at 90 °C. For all values of the electric field strengths, it was concluded that the dielectric constant has its maximum value at low frequencies, and then it begins to decrease rapidly as the frequency increases until it becomes almost constant at the high frequency range. At low frequencies, Nafion® 112 polarization is governed by two processes. The first process is the electronic polarization, which occurs as a result of the electron displacement inside the molecules in response to the electric field applied to the material. At the low frequencies, the ions have sufficient time to move and be aligned with the electric field; this can lead to a high value of ε' . In the second process, ionic polarization is formed from the movement of charged particles inside the material. Referring to Nafion® 112, a network of ion-rich channels is created as a result of the ionic groups, and these channels help in transferring the ions. As the frequency rises, the response time begins to drop. At high frequencies, the ions' response time is insignificant, resulting in a constant dielectric constant that reaches a plateau. This plateau represents the material's fundamental electrical characteristics. On the other hand, the rapid decrease in the dielectric constant of Nafion® 112 with increasing frequency is due to the constraints of its polarization processes. The oscillation of the electric field occurs too quickly for the dipoles to align properly, resulting in diminished polarization. As a result, orientation polarization becomes minimal, and dielectric losses may increase, lowering the effective dielectric constant due to the energy released as heat from delayed polarization responses [69,70].

The energy lost as heat when a substance is subjected to an alternating electric field is represented by the dielectric loss ε'' , and sometimes it is referred to as the loss tangent. When frequency increases in Nafion® 112, the dielectric loss typically falls quickly until reaching nearly constant levels at high frequencies, as shown in Figure 6b, which could be attributed to the relaxation process inside the material. At a low frequency, the molecules can respond to the electric field, which causes energy dissipation and increases the dielectric loss. Increasing the frequency leads to a decrease in the relaxation time, which suppresses the ability of the molecules to get oriented with the electric field. At a higher frequency, the responsibility of the relaxation process for the loss tangent occurs considerably fast during quite a short time. Relaxation processes in this range are generally associated with motions at smaller scales, including dipolar interactions or molecular rearrangements. At high frequencies, the dielectric loss becomes practically constant because the frequency of the applied field has little discernible effect on these rapid relaxation processes [62,71].

Figure 7a exhibits the influence of the frequency on the conductivity of the as-received sample after it was exposed to different strengths of electric field at 90 °C. Two frequency-dependent zones can be seen in Figure 7a. At low frequencies, the rapid increase in the conductivity is due to the polymer chains, which are aligned with the applied electric field; this leads to enhanced proton mobility. At high frequencies, the time of the relaxation process is quite limited, as was introduced above, and the molecules do not have the ability to respond to the electric field; as a result, the conductivity becomes almost constant [72].

Jonscher’s power law can describe the variation in the (alternative current, ac) conductivity with the frequency according to the following relation [73]:

$$\sigma_{ac} = A\omega^s, \tag{21}$$

where ω represents the angular frequency, A is a temperature dependence constant, and the slope of the straight line that resulted from the relation between conductivity and frequency can be used to compute the s -parameter.

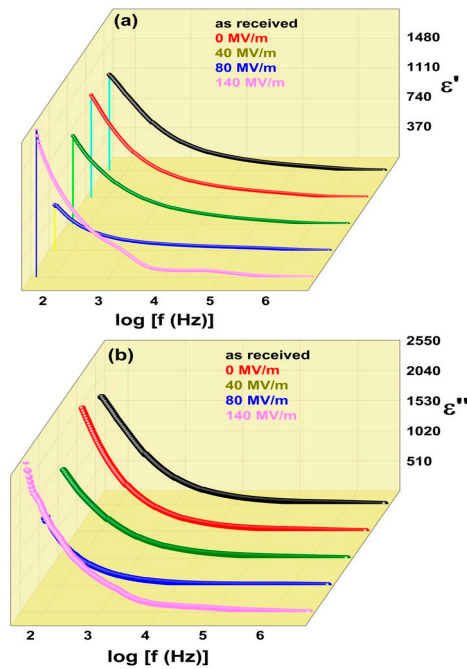


Figure 6. Variations in the (a) dielectric constant ϵ' and (b) dielectric loss ϵ'' with frequency for the as-received Nafion[®] 112 and Nafion[®] 112 exposed to different strengths of the applied electric field at 90 °C.

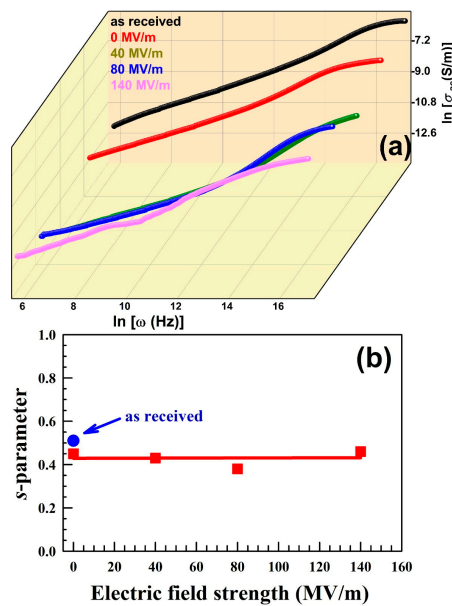


Figure 7. (a) The influence of the frequency on the ac conductivity, and (b) the variation in the Jonscher’s power law’s s -parameter with the applied electric field for the as-received Nafion[®] 112 and Nafion[®] 112 exposed to different strengths of the applied electric field at 90 °C.

The values of the s -parameter and its variation with the electric field strength are indicators of the conduction mechanism inside the sample. Figure 7b shows the variation in the s -parameter with the electric field strength. One can observe that the values of s -parameter are lower than unity with a slight decrease in the electric field strength. According to the s -parameter values, the primary conduction mechanism in the current samples is correlated barrier hopping (CBH). In the context of correlated barrier hopping, the energy differential that an electron must overcome to go from one side to another is represented by the barrier height. The likelihood of hopping between locations is determined by the barrier's height, which also affects the material's overall conductivity [74,75]. In the case of the CBH mechanism, the binding energy, or the barrier height, W_h , of charge carriers in their localized states is given as follows:

$$s = 1 - \frac{6KT}{W_h + KT \ln(\omega t_0)} \quad (22)$$

here W_h is the energy needed for the charged particles to overcome the barrier height and move inside the material, the Boltzmann constant is denoted by K , T represents the absolute temperature, and t_0 is the relaxation time. t_0 lies in the order of the vibrational period of an atom (of about 10^{-13} s) [71,76,77]. If $\ln(\omega t_0) \ll W_h$, then Equation (22) reads

$$s = 1 - \frac{6KT}{W_h} \quad (23)$$

Table 2 lists the calculated barrier height values W_h using Equation (23). Higher fields may further lower the effective barrier heights, improving the material's carrier mobility and overall conductivity, as evidenced by the slight decrease in the s -parameter as the electric field strength increases. In contrast to vehicle transport, which involves the movement of larger ionic species, and the Grotthuss mechanism, where proton hopping is the predominant transport process, the low barrier heights in the current study suggest a correlated barrier hopping mechanism that facilitates effective charge carrier transport. Reference [78] reported a similar behavior for $[(\text{CH}_3)_2\text{NH}_2]_2\text{CoCl}_4$. Increasing the applied electric field works to align the water molecules. This alignment reduces the energy barrier that protons need to overcome to move through the membrane. The aligned water molecules provide a favorable pathway for proton transport, lowering the effective barrier height.

Table 2. Variations in the barrier height with the electric field strength. See text for details.

Electric Field (MV/m)	Barrier Height, W_h (10^{-3} eV)
as received	0.310
0	0.282
40	0.272
80	0.250
140	0.287

Studying the complex impedance for a polymer helps to describe the grain and grain boundary interactions. Figure 8a shows the dependency of the real impedance Z' on the frequency for the as-received Nafion® and Nafion® 112 exposed to different strengths of the applied electric field at 90 °C. It is observed that, in the low frequencies, the real impedance decreases quickly with frequency, and then it gets saturated in the high frequency range. This reveals the variety of polarization in the membrane, such as orientational and electronic polarization behaviors. In addition, the appearance of the ac conductivity in the high-frequency region suppresses the ohmic effect [79]. Figure 8b illustrates the imaginary impedance Z'' , which also shows a decreasing trend with increasing frequency. Z'' represents the reactive component associated with capacitance and inductance in the system. At low frequencies, Z'' is observed to be higher, which is owing to the pronounced effects of dielectric polarization. The strong polarization effect at low frequencies results from

the ability of the charge carriers to respond to the external electric field, where they have enough time to do that. As the frequency increases, the responsibility of the charge carriers is diminished and leads to decreased polarization, which results in a decrease in Z'' . This aligns with the trend observed for Z' , where the overall impedance decreases.

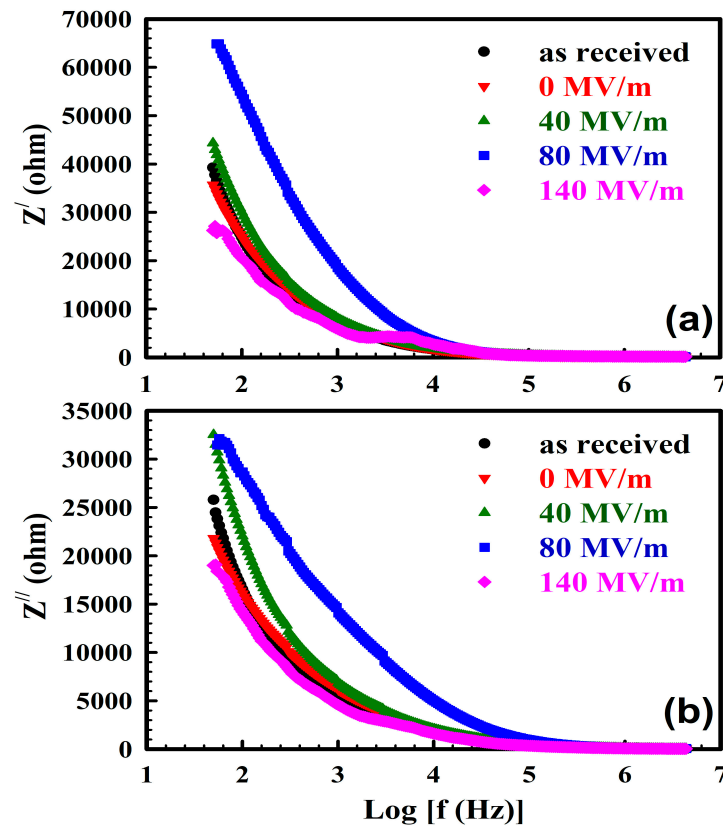


Figure 8. The frequency dependence of the (a) real impedance Z' and (b) imaginary impedance Z'' of the as-received Nafion[®] 112 and Nafion[®] 112 exposed to different strengths of the applied electric field at 90 °C.

To analyze the electrical properties of a material, the ac impedance method is the most suitable method to carry out such a study. Figure 9a exhibits the Nyquist plot of the investigated sample. Generally, for all the curves, one can observe a small semicircle in the high-frequency range followed by a tall spike in the low-frequency range. This shows that there is a different combination of the relaxation process; the semicircle represents smaller relaxation, while the spike represents faster relaxation. Also, the depressed semicircles in all curves confirm the non-Debye nature of the sample [80–83]. According to electrochemical impedance spectroscopy (EIS) software and spectroscopy [84], the bulk resistance R_b was obtained from fitting the Nyquist plot. R_b can be obtained from the intersection of the spike extension with the semicircle, the value of the intersected point on the Z' -axis is the bulk resistance [85–87]. The direct current (dc) conductivity, σ_{dc} , represents how a material can conduct the electric current depending only on its resistivity and temperature. σ_{dc} can be calculated as follows:

$$\sigma_{dc} = \frac{d}{a \cdot R_b}, \tag{24}$$

where a denotes the effective area of the sample and d denotes the sample thickness.

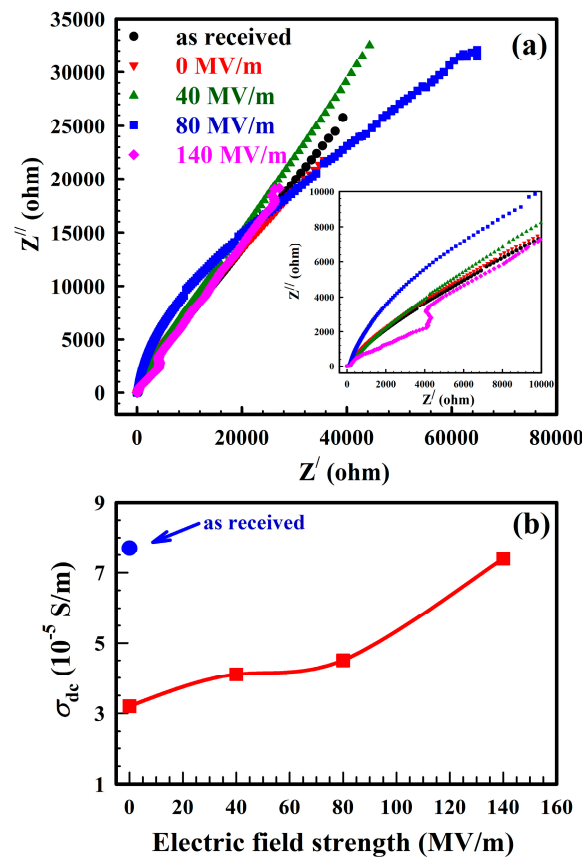


Figure 9. (a) Cole–Cole plot and (b) the dc conductivity σ_{dc} of the as-received Nafion[®] 112 and Nafion[®] 112 exposed to different strengths of the applied electric field at 90 °C.

Figure 9b shows the relation between the dc conductivity and the electric field of both the as-received membrane and after exposure to different electric field strengths at 90 °C. Firstly, it can be observed that σ_{dc} of the as-received Nafion[®] 112 is higher than that of Nafion[®] 112 heated at 90 °C. This is due to the partial leakage of the water content from Nafion[®] 112 with heating, especially in the temperature range from 80 to 100 °C [88]. Considering the effect of the applied electric field, the dc conductivity increases with increasing electric field strength. The electric field enhances the proton mobility within the membrane, where it can exert a force on the charged particles in the membrane, including protons. This force leads to the increased migration of ions, thereby increasing the overall conductivity of the membrane. On the other hand, the distribution of water molecules inside the Nafion[®] 112 membrane, which plays a significant role in proton conductivity, can be influenced by the applied electric field. Under the influence of the electric field, water molecules can migrate freer, facilitating proton transport and contributing to increased conductivity [72].

Figure 10 exhibits the free volume dependence of both the barrier height W_h and the dc conductivity σ_{dc} of the as-received Nafion[®] 112 and Nafion[®] 112 exposed to different strengths of the applied electric field at 90 °C. One can see from Figure 10a that the barrier height decreases slightly as the free volume increases. A larger free volume provides more pathways and less obstructed routes for the charge carriers to travel. Furthermore, the potential barriers experienced by the charge carriers become lower, reducing the overall barrier height. This makes it freer for the charge carriers to go through the material and facilitates charge transmission because it takes less energy to get past possible obstacles. It is commonly known that the free volume refers to the empty spaces or voids present within a material. In Nafion[®] 112, larger free volume sizes are typically associated with increased molecular mobility and enhanced ion transport. When the free volume size increases, there is more space available for ions, such as protons, to move through the membrane. This

enhanced mobility of ions results in better conductivity. As a result, an increase in the free volume size in Nafion[®] 112 is often related to an increase in conductivity, as illustrated in Figure 10b, consistent with the findings by two authors of this paper [89]. As evidenced by the pronounced correlations between the free volume and both the barrier height W_h and dc conductivity σ_{dc} , this confirms the significant role the free volume plays in the conductivity of Nafion[®] 112.

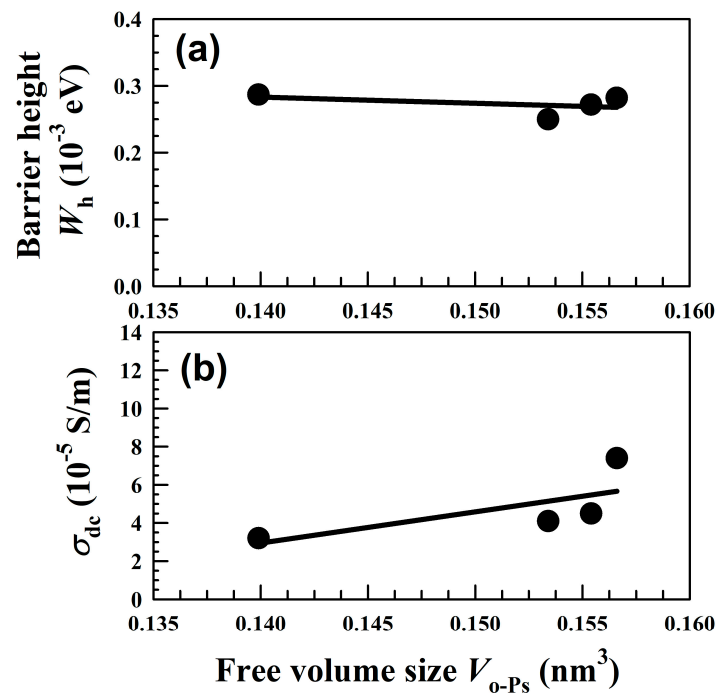


Figure 10. The correlations between the free volume size V_{o-Ps} and both the (a) barrier height W_h and (b) dc conductivity σ_{dc} of Nafion[®] 112 exposed to different strengths of the applied electric field at 90 °C. See text for details.

4. Conclusions

In this study, we investigated how an electric field influences the behavior of the Nafion[®] 112 membrane and its implications for the positron annihilation lifetime and proton conductivity. The experimental results demonstrated that the electric field intensity has a direct effect on the proton conductivity of the membrane, revealing a definite relationship between conductivity and the strength of the applied field. The correlated barrier hopping (CBH) mechanism was identified as the primary conduction mechanism within the investigated sample. Additionally, the analysis of the positron annihilation lifetime revealed distinct lifetime components, indicating variations in positron trapping sites and free volumes sizes within the membrane. These findings enhance the understanding of the electrical and structural characteristics of the Nafion[®] 112 membrane, which is crucial for optimizing its performance in applications such as fuel cells, electrochemical devices, and membrane separation. It was found that proton conductivity increased exponentially with the applied electric field, and that the size of the free volume reflected the increased mobility of ions as the degree of crystallinity decreased. The study confirmed that the free volume plays a significant role in both the barrier height and dc conductivity in Nafion[®] 112, as demonstrated by the strong linear correlations observed between the free volume size and both the barrier height and dc conductivity.

Author Contributions: Conceptualization, H.F.M.M. and E.E.A.-H.; methodology, W.M.M. and M.H.M.H.; validation, H.F.M.M., E.E.A.-H. and W.M.M.; formal analysis, M.H.M.H. and W.M.M.; investigation, H.F.M.M., E.E.A.-H. and W.M.M.; data curation, W.M.M. and M.H.M.H.; writing—original draft preparation, W.M.M. and M.H.M.H.; writing—review and editing, H.F.M.M. and E.E.A.-H.; supervision, H.F.M.M. and E.E.A.-H. All authors have read and agreed to the published version of the manuscript.

Funding: This research received no external funding.

Data Availability Statement: The datasets used and/or analyzed during the current study are available from the corresponding author upon reasonable request.

Conflicts of Interest: The authors declare no conflicts of interest.

References

1. Hsieh, T.-L.; Guo, W.-H.; Chang, M.-Y.; Huang, W.-Y.; Wen, H.-Y. Electric field-assisted filling of sulfonated polymers in ePTFE backing material for fuel cell. *Membr. J.* **2022**, *12*, 974. [[CrossRef](#)] [[PubMed](#)]
2. Sun, C.; Negro, E.; Vezzù, K.; Pagot, G.; Cavinato, G.; Nale, A.; Bang, Y.H.; Noto, V.D. Hybrid inorganic-organic proton-conducting membranes based on SPEEK doped with WO₃ nanoparticles for application in vanadium redox flow batteries. *Electrochim. Acta* **2019**, *309*, 311–325. [[CrossRef](#)]
3. Venkitesan Sakthivel, V.; Yoo, D.J. Enhanced solid-electrolyte interface efficiency for practically viable hydrogen-air fuel cell systems. *J. Energy Chem.* **2025**, *100*, 356–368. [[CrossRef](#)]
4. Mohamed, H.F.M.; Ito, K.; Kobayashi, Y.; Takimoto, N.; Takeoka, Y.; Ohira, A. Free volume and permeabilities of O₂ and H₂ in Nafion membranes for polymer electrolyte fuel cells. *Polymer* **2008**, *49*, 3091–3097. [[CrossRef](#)]
5. Mohamed, H.F.M.; Ohira, A.; Kobayashi, Y. Free volume and oxygen permeability in polymers related to polymer electrolyte fuel cells. *Mater. Sci. Forum* **2009**, *607*, 58–60. [[CrossRef](#)]
6. Mohamed, H.F.M. Positron annihilation techniques as probes for investigation of the polymer electrolyte membranes with different ion exchange capacities. *J. Egypt. Soc. Basic Sci.-Phys.* **2024**, *1*, 66–82. [[CrossRef](#)]
7. Mohamed, H.F.M.; Kobayashi, Y.; Kuroda, S.; Ohira, A. Positronium lifetimes and gas permeation in Aquivion[®] for fuel cells. *Mater. Sci. Forum* **2013**, *733*, 61–64. [[CrossRef](#)]
8. Mohamed, H.F.M.; Abdel-Hady, E.E.; Abdel-Hamed, M.O.; Said, M. Microstructure characterization of Nafion HP JP as a proton exchange membrane for fuel cell: Positron annihilation study. *Acta Phys. Pol. A* **2017**, *132*, 1543–1547. [[CrossRef](#)]
9. Mohamed, H.F.M.; Kuroda, S.; Kobayashi, Y.; Oshima, N.; Suzuki, R.; Ohira, A. Possible presence of hydrophilic SO₃H nanoclusters on the surface of dry ultrathin Nafion[®] films: A positron annihilation study. *Phys. Chem. Chem. Phys.* **2013**, *15*, 1518–1525. [[CrossRef](#)] [[PubMed](#)]
10. Sun, C.Y.; Zhang, H. Investigation of Nafion series membranes on the performance of iron-chromium redox flow battery. *Int. J. Energy Res.* **2019**, *43*, 8739–8752. [[CrossRef](#)]
11. Yin, C.; Li, J.; Zhou, Y.; Zhang, H.; Fang, P.; He, C. Phase separation and development of proton transport pathways in metal oxide nanoparticle/Nafion composite membranes during water uptake. *J. Phys. Chem. C* **2018**, *122*, 9710–9717. [[CrossRef](#)]
12. Maiti, T.K.; Maiti, T.K.; Singh, J.; Dixit, P.; Majhi, J.; Bhushan, S.; Bandyopadhyay, A.; Chattopadhyay, S. Advances in perfluorosulfonic acid-based proton exchange membranes for fuel cell applications: A review. *Chem. Engin. J. Adv.* **2022**, *12*, 100372. [[CrossRef](#)]
13. Tang, H.; Pan, M.; Wang, X.; Ruan, Y. Fabrication and characterization of PFSI/ePTFE composite proton exchange membranes of polymer electrolyte fuel cells. *Electrochim. Acta* **2007**, *52*, 5304–5311. [[CrossRef](#)]
14. Vinothkannan, M.; Kim, A.R.; Ramakrishnan, S.; Yu, Y.-T.; Yoo, D.J. Advanced Nafion nanocomposite membrane embedded with unzipped and functionalized graphite nanofibers for high-temperature hydrogen-air fuel cell system: The impact of filler on power density, chemical durability and hydrogen permeability of membrane. *Compos. B Engin.* **2021**, *215*, 108828. [[CrossRef](#)]
15. Lin, H.-L.; Yu, T.L.; Han, F.-H. A method for improving ionic conductivity of Nafion membranes and its application to PEMFC. *J. Polym. Res.* **2006**, *13*, 379–385. [[CrossRef](#)]
16. Mareev, S.; Gorobchenko, A.; Ivanov, D.; Anokhin, D.; Nikonenko, V. Ion and water transport in ion-exchange membranes for power generation systems: Guidelines for modeling. *Int. J. Mol. Sci.* **2023**, *24*, 34. [[CrossRef](#)] [[PubMed](#)]
17. Manso, A.P.; Marzo, F.F.; Barranco, J.; Garikano, X.; Mujika, M.G. Influence of geometric parameters of the flow fields on the performance of a PEM fuel cell. *Int. J. Hydrogen Energy* **2012**, *37*, 15256–15287. [[CrossRef](#)]
18. Teixeira, F.C.; de Sá, A.I.; Teixeira, A.P.; Rangel, C.M. Enhanced proton conductivity of Nafion-azolebisphosphonate membranes for PEM fuel cells. *New J. Chem.* **2019**, *43*, 15249–15257. [[CrossRef](#)]
19. Barique, M.A.; Tsuchida, E.; Ohira, A.; Tashiro, K. Effect of elevated temperatures on the states of water and their correlation with the proton conductivity of Nafion. *ACS Omega* **2018**, *3*, 349–360. [[CrossRef](#)] [[PubMed](#)]
20. Andersson, A.; Zhai, W.; Yu, J.; He, J.; Maurer, F.H. Free volume and crystallinity of poly (ethylene naphthalate) treated in pressurized carbon dioxide. *Polymer* **2010**, *51*, 146–152. [[CrossRef](#)]
21. Mohamed, H.F.M.; Abdel-Hady, E.E.; Mohamed, S.S. Temperature dependence of the free volume in polytetrafluoroethylene studied by positron annihilation spectroscopy. *Radiat. Phys. Chem.* **2007**, *76*, 160–164. [[CrossRef](#)]

22. Kamel, M.S.; Mohamed, H.F.M.; Abdel-Hamed, M.O.; Abdel-Hady, E.E. Characterization and evaluation of Nafion HP JP as proton exchange membrane: Transport properties, nanostructure, morphology, and cell performance. *J. Solid State Electrochem.* **2019**, *23*, 2639–2656. [[CrossRef](#)]
23. Mohamed, H.F.M.; Abdel-Hady, E.E.; Abdel-Hamed, M.O.; Kamel, M.S. Impact of ultraviolet radiation on the performance of polymer electrolyte membrane. *J. Solid State Electrochem.* **2020**, *24*, 1217–1229. [[CrossRef](#)]
24. Abdel-Hady, E.E.; Mohamed, H.F.M.; Abdel-Hamed, M.O.; Gomaa, M.M. Physical and electrochemical properties of PVA/TiO₂ nanocomposite membrane. *Adv. Polym. Technol.* **2018**, *37*, 3842–3853. [[CrossRef](#)]
25. El-Gamal, S.; El Sayed, A.M.; Abdel-Hady, E.E. Effect of cobalt oxide nanoparticles on the nano-scale free volume and optical properties of biodegradable CMC/PVA films. *J. Polym. Environ.* **2018**, *26*, 2536–2545. [[CrossRef](#)]
26. Gomaa, M.M.; Hugenschmidt, C.; Dickmann, M.; Abdel-Hady, E.E.; Mohamed, H.F.M.; Abdel-Hamed, M.O. Cross-linked PVA/SSA proton exchange membranes: Correlation of physiochemical properties with the free volume determined by positron annihilation spectroscopy. *Phys. Chem. Chem. Phys.* **2018**, *20*, 28287–28299. [[CrossRef](#)]
27. Ohira, A.; Kuroda, S.; Mohamed, H.F.M.; Tavernier, B. Effect of interface on surface morphology and proton conduction of polymer electrolyte thin films. *Phys. Chem. Chem. Phys.* **2013**, *15*, 11494–11500. [[CrossRef](#)]
28. Cooper, K. Progress toward accurate through-plane membrane resistance and conductivity measurement. *ECS Trans.* **2009**, *25*, 995–1007. [[CrossRef](#)]
29. Park, M.J.; Balsara, N.P. Anisotropic proton conduction in aligned block copolymer electrolyte membranes at equilibrium with humid air. *Macromolecules* **2010**, *43*, 292–298. [[CrossRef](#)]
30. Zhang, X.; Zhang, Y.; Nie, L.; Liu, X.; Chang, L. Modification of Nafion membrane by Pd-impregnation via electric field. *J. Power Sources* **2012**, *216*, 526–529. [[CrossRef](#)]
31. Taha, H.G.; Mohamed, H.F.M. Study of the nanostructure of γ -irradiated high-density polyethylene/carbon black composite and its durability as geo membrane. *Polym. Adv. Technol.* **2020**, *31*, 1581–1590. [[CrossRef](#)]
32. Mohamed, H.F.M.; Abdel-Hady, E.E.; Abdel-Hamed, M.O. Proton conductivity and free volume properties in per-fluorinated sulfonic acid/PTFE copolymer for fuel cell. *Acta Phys. Pol. A* **2017**, *132*, 1509–1514. [[CrossRef](#)]
33. Mohamed, H.F.M.; Kobayashi, Y.; Kuroda, C.S.; Ohira, A. Effects of ion-exchange on free volume and oxygen permeation in Nafion for fuel cells. *J. Phys. Chem. B* **2009**, *113*, 2247–2252. [[CrossRef](#)] [[PubMed](#)]
34. Okamoto, K.I.; Tanaka, K.; Katsube, M.; Sueoka, O.; Ito, Y. Positronium formation in various polyimides. *Radiat. Phys. Chem.* **1993**, *41*, 497–502. [[CrossRef](#)]
35. Kim, H.-J.; Kim, H.-J.; Krishnan, N.N.; Lee, S.-Y.; Hwang, S.Y.; Kim, D.; Jeong, K.J.; Lee, J.; Cho, E.; Lee, J.; et al. Sulfonated poly(ether sulfone) for universal polymer electrolyte fuel cell operations. *J. Power Sources* **2006**, *160*, 353–358. [[CrossRef](#)]
36. Kirkegaard, P.; Eldrup, M.; Mogensen, O.E.; Pedersen, N.J. Program system for analysing positron lifetime spectra and angular correlation curves. *Comput. Phys. Commun.* **1981**, *23*, 307–335. [[CrossRef](#)]
37. Olsen, J.V.; Kirkegaard, P.; Pedersen, N.J.; Eldrup, M. PALSfit: A new program for the evaluation of positron lifetime spectra. *Phys. Status Solidi C* **2007**, *4*, 4004–4006. [[CrossRef](#)]
38. Ito, K.; Oka, T.; Kobayashi, Y.; Shirai, Y.; Wada, K.; Matsumoto, M.; Fujinami, M.; Hirade, T.; Honda, Y.; Hosomi, H.; et al. Interlaboratory comparison of positron annihilation lifetime measurements for synthetic fused silica and polycarbonate. *J. Appl. Phys.* **2008**, *104*, 026102. [[CrossRef](#)]
39. Ito, K.; Oka, T.; Kobayashi, Y.; Shirai, Y.; Wada, K.; Matsumoto, M.; Fujinami, M.; Hirade, T.; Honda, Y.; Hosomi, H.; et al. Interlaboratory comparison of positron annihilation lifetime measurements. *Mater. Sci. Forum* **2009**, *607*, 248–250. [[CrossRef](#)]
40. Jean, J.Y.; Mallon, P.E.; Schrader, D.M. (Eds.) *Principles and Applications of Positron and Positronium Chemistry*; World Scientific Publishing Co. Pte. Ltd.: Singapore, 2003. [[CrossRef](#)]
41. Mohamed, H.F.M.; El-Sayed, A.M.A.; Hussien, A.Z. On irradiated poly (ethylene naphthalate) studied by positron annihilation lifetime spectroscopy. *Mater. Sci. Forum* **2001**, *363–365*, 325–327. [[CrossRef](#)]
42. Hmamm, M.F.M.; Zedan, I.T.; Mohamed, H.F.M.; Hanafy, T.A.; Bekheet, A.E. Study of the nanostructure of free volume and ionic conductivity of polyvinyl alcohol doped with NaI. *Polym. Adv. Technol.* **2021**, *32*, 173–182. [[CrossRef](#)]
43. Toa, S.T. Positronium annihilation in molecular substances. *J. Chem. Phys.* **1972**, *56*, 5499–5510. [[CrossRef](#)]
44. Eldrup, M.; Lightbody, D.; Sherwood, J.N. The temperature dependence of positron lifetimes in solid pivalic acid. *Chem. Phys.* **1981**, *63*, 51–58. [[CrossRef](#)]
45. Nakanishi, H.; Wang, S.-J.; Jean, Y.-C. Microscopic surface tension studied by positron annihilation. In *Positron Annihilation Studies of Fluids*; Sharma, S.C., Ed.; World Scientific Publishing Co. Pte. Ltd.: Singapore, 1988; pp. 292–298.
46. Kobayashi, Y.; Ito, K.; Oka, T.; He, C.; Mohamed, H.F.M.; Suzuki, R.; Ohdaira, T. Application of positron beams to the study of positronium-forming solids. *Appl. Surf. Sci.* **2008**, *255*, 174–178. [[CrossRef](#)]
47. Kansy, J. Microcomputer program for analysis of positron annihilation lifetime spectra. *Nucl. Instrum. Meth. Phys. Res. A Accel. Spectrom. Detect. Assoc. Equip.* **1996**, *37*, 235–244. [[CrossRef](#)]
48. Dlubek, G.; Supej, M.; Bondarenko, V.; Pionteck, J.; Pompe, G.; Krause-Rehberg, R.; Emri, I.; Dlubek, G. Ortho-positronium lifetime distribution analyzed with MELT and LT and free volume in poly (ecaprolactone) during glass transition, melting, and crystallization. *J. Polym. Sci. Polym. Phys.* **2003**, *41*, 3077–3088. [[CrossRef](#)]
49. El-Desoky, M.M.; Abdel-Hady, E.E.; Mohamed, H.F.M.; Hassanien, M.H.M.; Abdallah, N.; Harby, A.E. Annealing effects on the structural, positron annihilation parameters, and electrical properties of Fe₂O₃-PbO₂-TeO₂ glasses. *Phys. Scr.* **2024**, *99*, 035934. [[CrossRef](#)]

50. Elsharkawy, M.R.; Mohamed, H.F.M.; Hassanien, M.H.; Gomaa, M.M. Humidity effect on the transport properties of per-fluorinated sulfonic acid/PTFE proton exchange membranes: Positron annihilation study. *Polym. Adv. Technol.* **2022**, *33*, 952–965. [[CrossRef](#)]
51. Shpotyuk, O.; Adamiv, V.; Teslyuk, I.; Ingram, A. Positron lifetime spectroscopy of lithium tetraborate $\text{Li}_2\text{B}_4\text{O}_7$ glass. *J. Non-Cryst. Solids* **2017**, *471*, 338–343. [[CrossRef](#)]
52. Shantarovich, V.P.; Goldanskii, V.I. Positron annihilation in free volume elements of polymer structures. *Hyperfine Interact.* **1998**, *116*, 67–81. [[CrossRef](#)]
53. Lin, J.; Wycisk, R.; Pintauro, P.N.; Kellner, M. Stretched recast Nafion for direct methanol fuel cells. *Electrochem. Solid-State Lett.* **2007**, *10*, B19–B22. [[CrossRef](#)]
54. Mohamed, H.F.M.; Ito, Y.; Imai, M. Change of distribution of free volume holes during crystallization of poly(ethylene terephthalate) revealed by positron annihilation lifetime spectroscopy. *J. Chem. Phys.* **1996**, *105*, 4841–4845. [[CrossRef](#)]
55. Awad, S.; Abdel-Hady, E.E.; Mohamed, H.F.M.; Elsharkawy, Y.S.; Gomaa, M.M. Evaluation of transport mechanism and nanostructure of non-perfluorinated PVA/sPTA proton exchange membrane for fuel cell application. *Polym. Adv. Technol.* **2022**, *33*, 3339–3349. [[CrossRef](#)]
56. Mogensen, O.E. *Positron Annihilation in Chemistry*; Springer: Berlin/Heidelberg, Germany, 1995. [[CrossRef](#)]
57. Mohamed, H.F.M. Study of the effect of electric field on positron annihilation parameters in polymers. *Radiat. Phys. Chem.* **2003**, *68*, 449–452. [[CrossRef](#)]
58. Kobayashi, Y.; Mohamed, H.F.M.; Ohira, A. Positronium formation in aromatic polymer electrolytes for fuel cells. *J. Phys. Chem. B* **2009**, *113*, 5698–5701. [[CrossRef](#)] [[PubMed](#)]
59. Eldrup, M.; Jensen, K.O. Positron trapping rates into cavities in Al-temperature and size effects. *Phys. Stat. Sol. A* **1987**, *102*, 145–152. [[CrossRef](#)]
60. Dryzek, J. Application of positron annihilation spectroscopy studies of bismuth and subsurface zone induced by sliding. In *Bismuth—Advanced Applications and Defects Characterization*; Zhou, Y., Dong, F., Jin, S., Eds.; InTech: Rijeka, Croatia, 2018. [[CrossRef](#)]
61. Brandt, W.; Reinheimer, J. Impurity screening in amorphous semiconductors. *Phys. Lett. A* **1971**, *35*, 107–108. [[CrossRef](#)]
62. Mohammed, W.M.; Awad, S.; Abdel-Hady, E.E.; Mohamed, H.F.M.; Elsharkawy, Y.S.; Elsharkawy, M.R.M. Nanostructure analysis and dielectric properties of PVA/sPTA proton exchange membrane for fuel cell applications: Positron lifetime study. *Radiat. Phys. Chem.* **2023**, *208*, 110942. [[CrossRef](#)]
63. Havriliak, S.; Negami, S. A complex plane analysis of α -dispersions in some polymer systems. *J. Polym. Sci. C Polym. Symp.* **1966**, *14*, 99–117. [[CrossRef](#)]
64. Havriliak, S.; Negami, S. A complex plane representation of dielectric and mechanical relaxation processes in some polymers. *Polymer* **1967**, *8*, 161–210. [[CrossRef](#)]
65. Davidson, D.W.; Cole, R.H. Dielectric relaxation in glycerine. *J. Chem. Phys.* **1950**, *18*, 1417. [[CrossRef](#)]
66. Feldman, Y.; Puzenko, A.; Ryabov, Y. Non-Debye dielectric relaxation in complex materials. *Chem. Phys.* **2002**, *284*, 139–168. [[CrossRef](#)]
67. Shioya, Y.; Mashimo, S. Comparison between interpretations of dielectric behavior of poly (vinyl acetate) by the coupling model and the Havriliak–Negami equation. *J. Chem. Phys.* **1987**, *87*, 3173–3177. [[CrossRef](#)]
68. West, A.R. *Solid State Chemistry and Its Applications*; John Wiley & Sons, Inc.: New York, NY, USA, 2022.
69. Qin, M.; Zhang, L.; Wu, H. Dielectric loss mechanism in electromagnetic wave absorbing materials. *Adv. Sci.* **2022**, *9*, 2105553. [[CrossRef](#)] [[PubMed](#)]
70. Ahmed, K.; Kanwal, F.; Ramay, S.M.; Mahmood, A.; Atiq, S.; Al-Zaghayer, Y.S. High dielectric constant study of TiO_2 -polypyrrole composites with low contents of filler prepared by in situ polymerization. *Adv. Condens. Matter Phys.* **2016**, *2016*, 4793434. [[CrossRef](#)]
71. Mohamed, H.F.M.; Abdel-Hady, E.E.; Mohammed, W.M. Investigation of transport mechanism and nanostructure of Nylon-6,6/PVA blend polymers. *Polymers* **2022**, *15*, 107. [[CrossRef](#)]
72. Mohamed, H.F.M.; Hassanien, M.H.M.; Gomaa, A.G.R.; Aboud, A.A.A.; Ragab, S.A.M.; Ahmed, A.A.; Saeed, W.R.M. The electric field effect on the nanostructure, transport, mechanical, and thermal properties of polymer electrolyte membrane. *J. Polym. Res.* **2021**, *28*, 216. [[CrossRef](#)]
73. Abdel-Hamed, M.O.; Draz, A.A.; Khalaf, M.; El-Hossary, F.M.; Mohamed, H.F.M.; Abdel-Hady, E.E. Effect of plasma pretreatment and graphene oxide ratios on the transport properties of PVA/PVP membranes for fuel cells. *Sci. Rep.* **2024**, *14*, 1092. [[CrossRef](#)]
74. Ben Taher, Y.; Oueslati, A.; Maaloul, N.K.; Khirouni, K.; Gargouri, M. Conductivity study and correlated barrier hopping (CBH) conduction mechanism in diphosphate compound. *Appl. Phys. A Mater. Sci. Process.* **2015**, *120*, 1537–1543. [[CrossRef](#)]
75. Menyawy, E.M.; Zedan, I.T.; Nawar, H.H. Electrical conductivity and dielectric relaxation of 2-(antipyrin-4-ylhydrazono)-2-(4-nitrophenyl) acetonitrile. *Phys. B Condens. Matter* **2014**, *437*, 58–62. [[CrossRef](#)]
76. Banerjee, S.; Kumar, A. Dielectric behavior and charge transport in polyaniline nanofiber reinforced PMMA composites. *J. Phys. Chem. Solids* **2010**, *71*, 381–388. [[CrossRef](#)]
77. Mahmoud, K.H.; Abdel-Rahim, F.M.; Atef, K.; Saddeek, Y.B. Dielectric dispersion in lithium–bismuth–borate glasses. *Curr. Appl. Phys.* **2011**, *11*, 55–60. [[CrossRef](#)]
78. Mahfoudh, N.; Karoui, K.; Gargouri, M.; BenRhaïem, A. Optical and electrical properties and conduction mechanism of $[(\text{CH}_3)_2\text{NH}_2]_2\text{CoCl}_4$. *Appl. Organomet. Chem.* **2020**, *34*, e5404. [[CrossRef](#)]
79. Dhahri, A.; Dhahri, E.; Hlil, E.K. Electrical conductivity and dielectric behaviour of nanocrystalline $\text{La}_{0.6}\text{Gd}_{0.1}\text{Sr}_{0.3}\text{Mn}_{0.75}\text{Si}_{0.25}\text{O}_3$. *RSC Adv.* **2018**, *8*, 9103–9111. [[CrossRef](#)] [[PubMed](#)]

80. Lanfredi, S.; Saia, P.S.; Lebullenger, R.; Hernandez, A.C. Electric conductivity and relaxation in fluoride, fluorophosphate and phosphate glasses: Analysis by impedance spectroscopy. *Solid State Ion.* **2002**, *146*, 329–339. [[CrossRef](#)]
81. Priya, S.S.; Karthika, M.; Selvasekarapandian, S.; Manjuladevi, R. Study of biopolymer I-carrageenan with magnesium perchlorate. *Ionics* **2018**, *24*, 3861–3875. [[CrossRef](#)]
82. Abdel-Hady, E.E.; Gamal, A.; Hamdy, H.; Shaban, M.; Abdel-Hamed, M.O.; Mohammed, M.A.; Mohammed, W.M. Methanol electro oxidation on Ni–Pt–CrO/CNFs composite: Morphology, structural, and electrochemical characterization. *Sci. Rep.* **2023**, *13*, 4870. [[CrossRef](#)]
83. Awad, S.; Kaouach, H.; Mohammed, M.A.; Abdel-Hady, E.E.; Mohammed, W.M. Fabrication of bimetallic Ni-Ag/CNFs nanoparticles as a catalyst in direct alcohol fuel cells (DAFCs). *Polym. Adv. Technol.* **2023**, *34*, 1723–1738. [[CrossRef](#)]
84. Bondarenko, A.S.; Ragoisha, G.A. Inverse problem in potentiodynamic electrochemical impedance. In *Progress in Chemometrics Research*; Pomerantsev, A.L., Ed.; Nova Science Publishers, Inc.: New York, NY, USA, 2005; pp. 89–102.
85. Prado-Fernández, J.; Rodríguez-Vázquez, J.A.; Tojo, E.; Andrade, J.M. Quantitation of κ -, ι - and λ -carrageenans by mid-infrared spectroscopy and PLS regression. *Anal. Chim. Acta* **2003**, *480*, 23–37. [[CrossRef](#)]
86. Elsharkawy, M.R.; Mohammed, W.M. Effect of the electric field on the free volume investigated from positron annihilation lifetime and dielectric properties of sulfonated PVC/PMMA. *Polym. Adv. Technol.* **2024**, *35*, e6519. [[CrossRef](#)]
87. Elsharkawy, M.R.M.; Ibrahim, S.; Mohammed, W.M.M. Effect of V₂O₅ incorporation on the structural, electrical, and conduction properties of sulfonated PVC/PMMA blend: Positron annihilation study. *Egypt. J. Phys.* **2024**, *52*, 65–79. [[CrossRef](#)]
88. Avramov, S.G.; Lefterova, E.; Penchev, H.; Sinigersky, V.; Slavcheva, E. Comparative study on the proton conductivity of perfluorosulfonic and polybenzimidazole based polymer electrolyte membranes. *Bulg. Chem. Commun.* **2016**, *48*, 43–50. Available online: http://www.bcc.bas.bg/BCC_Content_Volume_48-B_Special.html (accessed on 21 November 2024).
89. Abdel-Hady, E.E.; Mohamed, H.F.M. Microstructure changes of poly(vinyl chloride) investigated by positron annihilation techniques. *Polym. Degrad. Stab.* **2002**, *77*, 449–456. [[CrossRef](#)]

Disclaimer/Publisher’s Note: The statements, opinions and data contained in all publications are solely those of the individual author(s) and contributor(s) and not of MDPI and/or the editor(s). MDPI and/or the editor(s) disclaim responsibility for any injury to people or property resulting from any ideas, methods, instructions or products referred to in the content.